Photoelectrocatalytic biosynthesis fueled by microplastics

Jinhyun Kim,[1] Jinha Jang,[1] Thomas Hilberath,[2] Frank Hollmann,[2] and Chan Beum Park[1]*

[1]Department of Materials Science and Engineering, Korea Advanced Institute of Science and Technology (KAIST), 335 Science Road, Daejeon 305-701, Republic of Korea
[2]Department of Biotechnology, Delft University of Technology, Van der Maasweg 9, 2629 HZ Delft, Netherlands *Email: parkcb@kaist.ac.kr

Abstract

Biocatalytic artificial photosynthesis integrates photocatalysis and redox biocatalysis through inspiration from plants to synthesize value-added chemicals using solar energy. The nature-inspired approach, however, suffers from sluggish rates due to the challenging water oxidation kinetics. Here, we report photoelectrochemical (PEC) biosynthetic reactions that use nonrecyclable real-world PET microplastics as an electron feedstock. A Zr-doped hematite photoanode (i) extracts electrons from hydrolyzed PET solutions obtained from post-consumer PET wastes (e.g., drinking bottles) and (ii) transfers the electrons to the bioelectrocatalytic site. Carbon-based cathodes receive the electrons to (i) activate redox enzymes [e.g., unspecific peroxygenase (UPO), L-glutamate dehydrogenase (GDH), ene-reductase from the old yellow enzyme family (OYE)] and (ii) drive various organic synthetic reactions, such as oxyfunctionalization of C-H bonds, amination of C=O bonds, and asymmetric hydrogenation of C=C bonds. These photoelectrocatalyst/biocatalyst hybrids achieve benchmark total turnover numbers of 362,000 (UPO), 144,000 (GDH), and 1,300 (OYE). This work presents a photoelectrocatalytic approach for integrating environmental remediation and biocatalytic photosynthesis towards sustainable solar-to-chemical synthesis.

1. Introduction

Plastics have become indispensable in our modern life; approximately 390 million tons of the polymers are produced worldwide annually.[1] The recent outbreak of the coronavirus pandemic has further stimulated global demand for plastics because of the increased usage of packaging materials and personal protective equipment.[2] The majority of plastic wastes have been incinerated or accumulated in landfills or the natural environment,[1] representing a severe loss of valuable resources (e.g., annual hemorrhage of 80 to 120 billion dollars to global economy).[3,4] Furthermore, microplastics—defined as plastics smaller than 5 mm—are imposing serious ecological and environmental threats.[1,5] Microplastics originate from the direct input from a variety of products (e.g., cosmetic beads, clothing fibers) or the degradation of plastic debris in the marine environment. Their small size and dilution hinder proper collection and reuse of microplastics, making them ubiquitous in oceans and even drinking water.[6]

Plastic recycling is desirable to address the issue but its execution is challenging because of mediocre waste management, deficiency of problem recognition, and complex chemical makeup.[3,4] For example, approximately 50% of poly(ethylene terephthalate) (PET) is not collected for recycling, although PET is the most abundant polyester plastic with an annual production of 38 million tons globally for textiles and packaging.[1] Only 7% of PET bottles are remolded into bottles, but recycling PET is still hampered by the loss of mechanical properties during the recycling process.[7] Chemical recycling has been considered as an alternative approach to convert nonrecyclable plastic wastes into valuable chemicals and materials.[3]

Here, we report a solar-driven biocatalytic photoelectrochemical (PEC) platform using nonrecyclable real-world PET microplastics as an electron feedstock to synthesize value-added compounds through the synergistic coupling of photoelectrocatalysis and redox biotransformations,

including oxyfunctionalization of C-H bonds, reductive amination of C=O bonds and *trans*-hydrogenation of conjugated C=C bonds. As depicted in **Fig. 1**, the biocatalytic PEC system consists of three components: (i) a zirconium-doped hematite (Zr:α-Fe$_2$O$_3$) photoanode to extract electrons from hydrolyzed PET solutions (from post-consumer commercial PET wastes from Starbucks and Coca-Cola companies), (ii) a carbon fiber paper (CFP) or anthraquinone-2-carboxylic acid (AQC)-anchored CFP cathode to generate 1,4-dihydronicotinamide adenine dinucleotide (1,4-NADH) or H$_2$O$_2$, respectively, and (iii) a redox enzyme [e.g., NADH-dependent L-glutamate dehydrogenase (GDH), NADH-dependent ene-reductase from the old yellow enzyme family (OYE), H$_2$O$_2$-dependent unspecific peroxygenase (UPO)] to drive synthetic reactions. The Zr:α-Fe$_2$O$_3$|CFP-based systems exhibit a broad applicability to other enzymatic substrates and high total turnover numbers (TTNs) of enzymes of 362,000 (UPO), 144,000 (GDH), and 1,300 (OYE), surpassing those of state-of-the-art biocatalytic PEC systems using water as an electron feedstock.

2. Results

2.1. Electrocatalytic reduction of antraquinone for biocatalytic oxyfunctionalization

We tested a CFP electrode for reductive activation of redox enzymes. The rationale of selecting CFP was its high electrical conductivity, large surface area, high chemical stability and good mechanical strength.[8] The CFP electrode exhibited randomly oriented microfibers with carbon-based functional groups (e.g., conjugated C=C, C-C, C-OH, and COOH). In depth structural characterization via scanning electron microscopy (SEM), X-ray photoelectron spectroscopy (XPS) and Raman spectroscopy are shown in Supplementary Information (**Supplementary Fig. 1**).

For the electrocatalytic production of H$_2$O$_2$, we prepared an AQC/CFP electrode via a solution immersion process (see the details in Methods section). The redox behavior of AQC on the

CFP was confirmed using cyclic voltammetry (CV) under reaction conditions representative for peroxygenase reactions[9] [100 mM potassium phosphate (KPi) buffer, pH 6.0]. The AQC/CFP exhibited a redox wave with a formal potential of *ca.* 0.1 V vs. reversible hydrogen electrode (V_{RHE}) under Ar-enriched environments, whereas the bare CFP did not show the characteristic redox peak (**Fig. 2a**). We attribute the wave to a typical two-electron-two-proton reduction/oxidation[10] of $AQC/AQCH_2$. The surface concentration of AQC was estimated to be 18 nmol cm^{-2} from its cyclic voltammogram. Upon purging the electrolyte solution with O_2, the cathodic current of the AQC/CFP was much higher than that of the CFP (**Fig. 2a**), indicating reoxidation of $AQCH_2$ via O_2 reduction.

We confirmed the role of AQC in promoting the reduction of O_2 to H_2O_2. As shown in **Fig. 2b**, the rate of H_2O_2 production in the AQC/CFP system was 1.85 ± 0.07 mM h^{-1} at 0.16 V_{RHE}. The rate decreased to 0.90 ± 0.04 mM h^{-1} in the absence of AQC. We attribute to the different rates of H_2O_2 generation to AQC-driven facilitation of the interfacial electron transfer process; our electrochemical impedance spectroscopic analysis shows that the charge transfer resistance of AQC/CFP is lower than that of CFP under O_2-rich conditions (**Supplementary Fig. 2 and Supplementary Table 1**). Under anaerobic conditions, H_2O_2 formation was negligible (< 0.06 mM h^{-1}) (**Supplementary Fig. 3**). We further confirmed that AQC/CFP-driven formation of H_2O_2 proceeds via a two-step, single-electron reduction of O_2 (**Supplementary Fig. 4**).

Having demonstrated *in situ* H_2O_2 production by the AQC/CFP cathode, we advanced to coupling AQC/CFP-driven electrocatalysis with peroxygenase-catalyzed oxyfunctionalization reactions. We selected the recombinant, evolved peroxygenase from *Agrocybe aegerita* (r*Aae*UPO), which exhibits a high activity towards oxidation of C-H bonds[11]. Selective oxyfunctionalization reactions of non-activated C-H bonds are very challenging in synthetic chemistry because of the kinetically inert nature of C-H bonds;[11] peroxygenases represent promising catalysts for challenging

4

oxyfunctionalization reactions because they combine high catalytic activity with high selectivity while depending on simple H_2O_2 only as oxidant. The application of $0.16\ V_{RHE}$ to AQC/CFP cathode drove hydroxylation of ethylbenzene to enantiopure (*R*)-1-phenylethanol [enantiomeric excess (*ee*) > 99%] with a formation rate of 1.63 ± 0.08 mM h^{-1}, corresponding to a turnover frequency of r*Aae*UPO (TOF$_{rAaeUPO}$) of $32,700 \pm 1,500$ h^{-1} (**Fig. 2c**). Control experiments in the absence of r*Aae*UPO, substrate, or electrical bias did not produce the enzymatic product (**Fig. 2c**).

2.2. Electrocatalytic regeneration of NADH for enzymatic amination and hydrogenation

We examined electrocatalytic capability of CFP to regenerate enzymatically active 1,4-NADH from NAD$^+$. [Cp*Rh(bpy)H_2O]$^{2+}$ (**M$_{ox}$**, Cp* = C_5Me_5, bpy = 2,2'-bipyridine) was used as a regeneration catalyst to attain highly regioselective reduction of NAD$^+$ into 1,4-NADH according to the literature.[12] Our linear sweep voltammograms showed a cathodic current of **M$_{ox}$** in an O_2-depleted sodium phosphate (NaPi) buffer (100 mM, pH 7.5) (**Fig. 2d**). The addition of NAD$^+$ further increased the cathodic current, indicating a catalytic effect of **M** in the electron transfer from CFP to NAD$^+$. However, the CFP cathode did not generate cathodic current by NAD$^+$ without **M$_{ox}$** (**Supplementary Fig. 5**), indicating imperceptible direct reduction of NAD$^+$. We further confirmed CFP-driven conversion of NAD$^+$ to 1,4-NADH using **M$_{ox}$**; our ^1H nuclear magnetic resonance (NMR) spectra exhibits a NADH's characteristic peak at 6.94 parts per million when we performed controlled potential electrolysis at $-0.2\ V_{RHE}$ (**Fig. 2e and Supplementary Fig. 6**). The rate of NADH production was 1.19 ± 0.07 mM h^{-1} at the electrical bias, which we estimated using UV-Vis spectroscopy. Control experiments in the absence of **M$_{ox}$**, NAD$^+$, or electrical bias did not produce NADH (**Fig. 2f**).

We applied the electrocatalytic regeneration system to activate GDH from bovine liver; GDH has been reported to receive electrons from NADH for the reductive amination reaction of α-ketoglutarate to L-glutamate[13], which is a global food flavor enhancer[14], a crop protection agent[15], and a livestock nutrient[16]. As shown in **Fig. 2g**, L-glutamate was formed with a rate of 2.74 ± 0.11 mM h^{-1} and a TOF$_{GDH}$ of $3,900 \pm 200$ h^{-1} at -0.2 V$_{RHE}$; the rate of enzymatic reaction was higher than those of NADH formation reaction (**Fig. 2f**), which has been observed in reports[13,17,18] on GDH catalysis driven by NADH regeneration. We may attribute it to faster regeneration of NADH driven by NADH-consuming GDH. The omission of **M$_{ox}$**, NAD$^+$, or GDH resulted in a negligible amount of L-glutamate (**Fig. 2g**), which indicates the electron transport from CFP to GDH through NADH regeneration process.

Furthermore, we revealed general applicability of the NADH regeneration system by coupling it with OYE-driven asymmetric hydrogenation reactions. In this experiment, we used an OYE from *Thermus scotoductus* (*Ts*OYE), catalyzing the enantioselective *trans*-hydrogenation of C=C bonds[19,20]. In addition, we replaced a NaPi buffer with a triethanolamine-buffered solution[19] (100 mM, pH 7.5; see the rationale for alteration in the Methods section); the rate of NADH formation remained constant regardless of the electrolyte type (**Supplementary Fig. 7**). Controlled potential electrolysis at -0.2 V$_{RHE}$ resulted in enzymatic conversion of 2-methyl-2-cyclohexen-1-one to (*R*)-2-methylcyclohexanone (*ee* > 99%) with a rate of 1.16 ± 0.16 mM h^{-1} and a TOF$_{Ts OYE}$ of 230 ± 30 h^{-1} (**Fig. 2h**). The rate of enzymatic reaction was similar than that of NADH regeneration reaction (**Supplementary Fig. 7**). The bioelectrocatalytic reaction required **M$_{ox}$**, NAD$^+$, *Ts*OYE, and electrical bias (**Fig. 2h**).

2.3. Photoanodic electron extraction from microplastics

To provide electrons for the CFP-based cathodes, we chose α-Fe$_2$O$_3$ because of its (i) earth-abundance (Fe and O as the fourth and first most abundant elements in the Earth's crust, respectively),[21] (ii) non-toxicity,[21] and (iii) excellent PEC stability under alkaline conditions (pH 13.6)[21], compared with visible-light-absorbing metal oxide semiconductors [e.g., BiVO$_4$ (unstable at pH > 11)[22], WO$_3$ (unstable at pH > 4)[23]]. We synthesized a α-Fe$_2$O$_3$ photoelectrode by (i) hydrothermally depositing akaganeite (β-FeOOH) on a fluorine-doped tin oxide substrate and (ii) thermally converting β-FeOOH into worm-like α-Fe$_2$O$_3$ (90 ± 12 nm in diameter, 312 ± 91 nm in length; **Figs. 3a and 3b**). Characterization details using analytical tools (e.g., SEM, XPS, X-ray diffraction) are shown in **Figs. 3a and 3b and Supplementary Fig. 8** and their legends. We investigated its optical and electronic properties because these photophysical properties determine PEC efficiencies. According to our ultraviolet-visible spectroscopy, the α-Fe$_2$O$_3$ absorbed ultraviolet and visible light below approximately 580 nm with a bandgap of 2.00 eV (**Supplementary Figs. 8f and 8g**). From α-Fe$_2$O$_3$'s ultraviolet photoelectron spectrum, we estimated its valence band edge potential, and conduction band edge potential to be 2.52 and 0.52 V$_{RHE}$, respectively (**Fig. 3c and Supplementary Figs. 8g and 8h**).

We investigated α-Fe$_2$O$_3$'s PEC performance on electron extraction from PET microplastics for different conditions at 303 K: (i) no bias under dark, (ii) anodic bias (1.0 V$_{RHE}$) under dark, (iii) no bias under solar light [air mass 1.5 global (AM 1.5G); 100 mW cm^{-2}], and (iv) the anodic bias under solar light. Note that the photoelectrocatalytic experiments began immediately as soon as we prepared an unpretreated PET solution by adding PET microplastics (size ≤ *ca*. 5 mm) in aqueous 5 M NaOH electrolyte solution (1 mg mL^{-1}; see Methods section for details). Quantitative ^{1}H NMR spectroscopy of the PET showed the solubilization of PET to ethylene glycol (EG) and benzene-1,4-dicarboxylate (BD) in conditions (i), (ii), and (iii) (**Supplementary Fig. 9**), which we attribute to

the alkaline hydrolysis of PET's ester functional groups. In stark contrast, the positive group—condition (iv)—resulted in the formation of 530 ± 23 nmol formate and 185 ± 9 nmol acetate (**Supplementary Fig. 9a**). These results signify that $\alpha\text{-Fe}_2\text{O}_3$ photoanode extracts electrons and produces organic fuels from solubilized nonrecyclable microplastics.

2.4. Mechanistic investigation

We performed mechanistic analyses to examine the underlying photoredox chemistry driven by $\alpha\text{-Fe}_2\text{O}_3$. For the analyses, we constructed a two-compartment, three-electrode configuration using a salt bridge, which maintains electrical neutrality within the internal circuit. We confirmed that PET reformation occurs through the photooxidative pathway; as shown in **Supplementary Fig. 10a**, we detected formate and acetate in the anodic site, not the cathodic site. Because the photoanode generated photoexcited holes, O_2, H_2O_2, and $OH^\bullet$ (**Supplementary Fig. 10b**), we investigated which species drove the waste-to-chemical conversion. As shown in **Fig. 3c**, the addition of Na_2SO_3 (hole scavenger) suppressed the reaction, whereas (i) the presence of sodium pyruvate (H_2O_2 scavenger) or *tert*-butyl alcohol ($OH^\bullet$ radical scavenger) and (ii) the purging with N_2 gas did not restrain the formation of formate and acetate. Note that H_2O_2 and O_2 themselves do not execute the target reaction under dark conditions without electrical bias (**Supplementary Fig. 10c**). These results indicate that photoexcited hole is solely responsible for the photooxidative reaction.

Because the alkaline solubilization of PET microplastics resulted in a formation of EG and BD (**Supplementary Fig. 9b**), we investigated which molecules reacted with $\alpha\text{-Fe}_2\text{O}_3$'s photoexcited holes. Our ^1H and ^{13}C NMR spectroscopic analyses show that photoelectroactivated $\alpha\text{-Fe}_2\text{O}_3$ oxidizes EG to a variety of products (**Supplementary Figs. 11a and 11b**). The oxidation products included C2 intermediates (e.g., glyoxal, glycolate, glyoxylate) and C1 products (e.g.,

formate, acetate). The oxidation intermediates were reported[24,25] to be (i) formed through the oxidation reaction of EG, and (ii) further oxidized to formate and acetate under alkaline conditions. The photoactivated α-Fe$_2$O$_3$ oxidized the C2 intermediates to formate and acetate (**Supplementary Figs. 11c, 11d, and 11e**). On the other hand, α-Fe$_2$O$_3$ did not oxidize BD during the PEC reaction (**Supplementary Fig. 11f**), which we attribute to the difficulty of oxidizing stable aromatic moieties.

We observed the dependency of PEC oxidation rates on applied bias and PET concentration. In the kinetic experiments, we prepared a pretreated PET solution (5 mg mL^{-1}; see the Methods section for the details) to use it as an electrolyte solution; this pretreatment step solubilizes the solid wastes in advance, which facilitates contact between the photoelectrocatalyst and the substrates. Our linear sweep voltammetric analysis shows that anodic currents of α-Fe$_2$O$_3$ increase with increasing applied bias and PET concentration under light conditions, not dark conditions (**Supplementary Figs. 12a and 12b**). Consistent with the result, the production rate of formate and acetate increased with increasing applied bias from 0.7 to 1.2 V$_{RHE}$ and PET concentration from 0 to 10 mg mL^{-1} (**Supplementary Figs. 12c and 12d**).

2.5. Hematite doping for enhanced photoanodic reactions

The separation of photoexcited charge carriers plays a decisive role in the efficiency of photoelectrocatalytic reactions because it increases the concentration of charge carriers that participate in a photoredox reaction. We hypothesized that doping treatment of α-Fe$_2$O$_3$ can boost the efficiency of the waste-to-chemical reaction because the strategy (i) increases electron concentration to enhance electrical conductivity and suppress charge recombination, and (ii) makes α-Fe$_2$O$_3$'s band bending more upward to provide a strong driving force for charge separation.[26,27] Thus, we introduced Zr^{4+} atoms into the α-Fe$_2$O$_3$ nanostructure to synthesize a Zr-doped α-Fe$_2$O$_3$

(Zr:α-Fe$_2$O$_3$) photoanode because the dopant[28] is reported to (i) provide electrons for α-Fe$_2$O$_3$ and (ii) accelerate electron transport between Fe atoms, in terms of small polaron model as conduction mechanism, which are beneficial for increasing carrier conductivity. The Zr doping insignificantly altered the phase, morphology, optical bandgap, and band edge potentials of the photoanode (**Supplementary Fig. 13** and its legend).

We observed the enhanced PEC performance of the Zr:α-Fe$_2$O$_3$; the photoanodic current of Zr:α-Fe$_2$O$_3$ increased considerably and the onset potential of water oxidation was cathodically shifted by 0.18 V when we used 2 mM Zr^{4+} ions in the precursor solution (**Supplementary Fig. 14**). We attribute the improved performance to (i) increased electron concentration (**Supplementary Fig. 15a**), (ii) enhanced charge separation dynamics (**Supplementary Fig. 15b**), (iii) decreased charge-transfer resistances at Zr:α-Fe$_2$O$_3$ interface (**Supplementary Figs. 15c and 15d**), (iv) suppressed charge recombination (**Supplementary Fig. 16**), and (v) more upward band bending (**Supplementary Fig. 15a**), which we obtained using (transient) voltammetric analysis, Mott-Schottky analysis, and electrochemical impedance spectroscopy. Detailed analytical results are shown in Supplementary Information (**Supplementary Figs. 15 and 16** and their legends).

These photophysical improvements caused by Zr doping resulted in a faster PET reformation. **Fig. 3d** displays that the Zr:α-Fe$_2$O$_3$ exhibits a faster production of formate and acetate than does the α-Fe$_2$O$_3$ photoanode from 0.8 to 1.2 V$_{RHE}$. Consistent with the results, the Zr:α-Fe$_2$O$_3$ photoanode generated a higher photoanodic current than α-Fe$_2$O$_3$ did under the same PET concentrations (**Fig. 3e**), which is beneficial to faster electron transport to CFP-based cathodes for rapid biocatalytic reactions.

We confirmed Zr:α-Fe$_2$O$_3$'s robust photoelectrocatalytic stability. As shown in **Supplementary Fig. 17a**, Zr:α-Fe$_2$O$_3$ exhibited a steady formation rate of formate and acetate

during a four-iteration experiment (12-h reaction per cycle). In addition, Zr:α-Fe$_2$O$_3$'s phase and surface chemical states did not alter and its constituent atoms did not leak into an electrolyte solution after the reusability test (**Supplementary Figs. 17b and 17c and Supplementary Tables 2 and 3**). These results indicate its propriety in long-term photoelectrocatalytic reactions.

Furthermore, we revealed the real-world applicability of the Zr:α-Fe$_2$O$_3$ energy material using microplastics from post-consumer PET wastes including a PET disposable cup from Starbucks coffee company and a PET bottle from Coca-Cola company (**Supplementary Figs. 18a and 18b**). The application of solar energy (1 sun) and electrical bias (1.1 V$_{RHE}$) to the photoanode triggered the formation of approximately 1.7 mmol formate and 40 μmol acetate from an unprehydrolyzed Starbucks PET cup and a Coca-Cola PET bottle for 10 days (**Supplementary Figs. 18c-18f**).

2.6. Photobiocatalytic synthesis fueled by real-world microplastics

Having substantiated CFP-mediated biosynthetic reactions and Zr:α-Fe$_2$O$_3$-driven transformation reactions, we integrated these two redox reactions in a two-compartment, two-electrode configuration (working electrode: Zr:α-Fe$_2$O$_3$ photoanode, counter electrode: AQC/CFP or CFP cathode). We prepared a pretreated PET solution—using microplastics from Starbucks PET cup— as an anodic electrolyte solution. The controlled potential photoelectrolysis triggered biocatalytic synthesis, including (i) r*Aae*UPO-driven production of enantiopure (*R*)-1-phenylethanol (**Fig. 4a**), (ii) GDH-driven formation of L-glutamate (**Fig. 4b**), and (iii) *Ts*OYE-catalyzed generation of enantiopure (*R*)-2-methylcyclohexanone (**Fig. 4c**). The enantioselectivities remained constant (*ee* > 99%) regardless of the scale of applied bias (**Figs. 4a and 4c**). Sheltering the PEC system from solar light made the synthetic reactions sluggish or imperceptible (**Fig. 4**), signifying that solar energy is a key energy resource to drive the redox reactions in a meaningful rate. We also revealed that rates

of photobiosynthetic reactions increased with PET concentration from 0 to 50 mg mL^{-1} (**Supplementary Fig. 19**), which indicates that PET provides electron donors (e.g., EG) for boosting enzymatic transformation reactions.

Using optimized applied bias of each enzymatic reaction, our photobiocatalytic system exhibited a TTN$_{rAaeUPO}$ of 113,000 (3 h), a TTN$_{GDH}$ of 144,000 (56 h), and a TTN$_{TsOYE}$ of 1,300 (7 h) (**Fig. 5 and Supplementary Fig. 20a**). The reaction times of GDH and *Ts*OYE were longer than those reported in precedent research on biocatalytic PEC systems[13,29-31], which we attribute to the robustness of the Zr:α-Fe$_2$O$_3$|CFP system and the biocatalysts. However, the r*Aae*UPO reaction halted at *ca.* 2 h (**Supplementary Fig. 20a**), which was shorter than that recorded in a previous biocatalytic PEC study[32]. We found that the CFP cathode formed OH$^•$ radicals (**Supplementary Fig. 20b**), which are reported[32,33] to readily deactivate the enzyme. Because electrochemical reduction of H$_2$O$_2$ forms OH$^•$ radicals [H$_2$O$_2$ + e$^-$ → OH$^•$ + OH$^-$, E_{red} = 0.79 V$_{RHE}$][32], we decreased the applied bias from 1.2 to 0.9 V, which resulted in a negligible formation of the radical (**Supplementary Fig. 20b**). This strategy resulted in a steady biosynthetic reaction with a TTN$_{rAaeUPO}$ of 271,000 (7 h) (**Fig. 5 and Supplementary Fig. 20a**). Zr:α-Fe$_2$O$_3$ produced formate and acetate during the photoelectrocatalytic reactions (**Supplementary Table 4**), which indicates the production of value-added compounds simultaneously at the anodic and cathodic sites.

We demonstrated a broad applicability of the photobiosynthetic platform by extending the substrate scope (**Supplementary Table 5**). **Fig. 5** displays (i) r*Aae*UPO-mediated synthesis of (*R*)-1,2,3,4-tetrahydro-1-naphthol (*ee* > 99%, TOF: 48,000 h^{-1}, TTN: 312,000), cyclohexanol (TOF: 36,000 h^{-1}, TTN: 234,000), and (1*R*, 2*S*)-1-phenylpropylene oxide (*ee* > 99%, TOF: 64,000 h^{-1}, TTN: 362,000) and (ii) *Ts*OYE-driven production of cyclohexanone (TOF: 420 h^{-1}, TTN: 1,300) and 3-phenylpropionaldehyde (TOF: 140 h^{-1}, TTN: 690). The biocatalytic PEC platform compares

favorably with the state-of-the-art biocatalytic PEC systems in a two-electrode configuration (**Fig. 6**). The reported PEC cells[13,30-32] extracted electrons from water to trigger redox biotransformations driven by rAaeUPO (TTN$_{\text{r}Aae\text{UPO}}$ < 50,000)[31,32], GDH (TTN$_{\text{GDH}}$: 108,000)[13], or TsOYE (TTN$_{Ts\text{OYE}}$ < 256)[30,31]. Our photoelectrocatalytic system acquired electrons from hydrolyzed PET solutions and accelerated enzymatic synthetic reactions with the highest TTN$_{\text{enzyme}}$ (TTN$_{\text{r}Aae\text{UPO}}$: 362,000, TTN$_{\text{GDH}}$: 144,000, TTN$_{Ts\text{OYE}}$: 1,300) among the solar-driven biocatalytic PEC systems.

3. Discussion

Inspired by natural photosynthesis, biocatalytic PEC platforms synthesize value-added compounds through the synergistic coupling of photoelectrocatalysis and redox biotransformations[12,34]. Mechanistically, a photoelectrode absorbs solar light and transfers its photoexcited charge carriers to the catalytic center of redox enzymes, which subsequently catalyze synthetically useful redox reactions (e.g., asymmetric hydrogenation of C=C bonds, amination of C=O bonds, hydroxylation of C-H bonds, epoxidation of C-H bonds)[12]. Biocatalytic PEC system has emerged as an alternative platform to biocatalytic photochemical system due to its merits[12,31,34], such as (i) suppression of undesirable back electron transfer and electron-hole recombination, (ii) independent examination of cathodic and anodic reactions, (iii) design of individual redox (photo)electrocatalysts, (iv) physical separation of anodic and cathodic sites, and (v) facile reusability of catalytic electrodes.

The majority of biocatalytic PEC systems[13,30,32,35,36] have focused water oxidation to provide the reducing equivalents needed to drive reductive enzymatic reactions. However, water oxidation poses significant limitations, such as its sluggish reaction rate caused by anodic four-electron (or two-electron) process[19] and the relatively low value of dioxygen[37]. This issue made us hypothesize

that finding another electron feedstock would accelerate enzymatic synthetic reactions and produce value-added chemicals simultaneously on oxidation and reduction sites.

The current work first demonstrates that real-world microplastics can provide electron feedstocks to expedite photobiosynthetic reactions with excellent TTNs. The two-compartment biocatalytic PEC system provides distinct advantages that are impossible in photocatalytic processes using homogeneous or heterogeneous photocatalysts: (i) flexible combination of redox reactions (e.g., EG oxidation with H_2O_2 production and NADH regeneration) with different reaction conditions [e.g., KPi buffer (pH 6.0) with NaOH alkaline solution], (ii) spatial separation of enzymatic products [e.g., (*R*)-1-phenylethanol, L-glutamate, (*R*)-2-methylcyclohexanone] and oxidation products (e.g., formate, acetate), (iii) protection of reduced electron mediators (e.g., **M**$_{\textbf{red}}$, NADH) and enzymes from photooxidation, (iv) control of applied bias to drive redox reactions selectively (e.g., H_2O_2 production without $OH^\bullet$ generation), and (v) development of individual (photo)electrodes (e.g., Zr:α-Fe_2O_3, AQC/CFP). Follow-up studies are needed to ameliorate the photoanodic performance of electron extraction through, for example, (i) modification of surface morphology to decrease charge recombination and (ii) construction of junctions to improve charge separation. In addition, functionalization of cathodes with additional catalysts would accelerate enzymatic reactions by boosting interfacial charge transfer to enzyme activators. These attempts will further expand the scope of our approach to other redox enzymatic reactions (e.g., hydrogenase-driven evolution of H_2, Baeyer-Villiger monooxygenase-mediated formation of esters and lactones) with improved efficiencies.

4. Conclusions

This study reports solar-assisted e-biorefinery approach that uses PET microplastics as an electron feedstock for redox biosynthesis. The Zr:α-Fe$_2$O$_3$|AQC/CFP and Zr:α-Fe$_2$O$_3$|CFP hybrids produced value-added chemicals at the anodic and cathodic sites through simultaneous enzymatic synthetic reactions (e.g., rAaeUPO-driven hydroxylation/epoxidation, GDH-mediated amination, and TsOYE-catalyzed hydrogenation) and EG oxidation. The photoanodic half-reaction by α-Fe$_2$O$_3$ led to (ii) extracted electrons to the CFP-based cathodes, and (i) yielded valuable chemicals (e.g., formate and acetate). To accelerate the photoanodic extraction of electrons, we synthesized the Zr:α-Fe$_2$O$_3$ photoanode that exhibited improved charge separation efficiencies ($\Delta\eta_{bulk}$ of 3.5 to 10%, $\Delta\eta_{surface}$ of 15 to 60%), decreased charge-transfer resistance (by up to 17 times), cathodic shift of flat-band potential by 0.16 V, and reduced charge recombination behaviors. Furthermore, the Zr:α-Fe$_2$O$_3$ photoanode reformed real-world PET samples, including PET microplastics from Starbucks and Coca-Cola's commercial PET items for over 10 days. The microplastic-fueled PEC biocatalysis showed a broad applicability to various enzymatic substrates and achieved benchmark performances (TTN$_{rAaeUPO}$: 362,000, TTN$_{GDH}$: 144,000, TTN$_{TsOYE}$: 1,300).

5. Methods

Characterization of carbon fiber paper. We bought a commercial carbon fiber paper (CFP) from HanTech (Korea). Before performing any experiments, we washed CFP using deionized water, ethanol, and acetone, and dried it under vacuum at room temperature. We used an ultra-high resolution scanning electron microscope SU8230 (Hitachi High-Tech Corp., Japan) to observe the morphology of the CFP. We employed a K-Alpha X-ray photoelectron spectrometer (ThermoFisher Scientific Inc., USA) to investigate chemical states of the CFP. We obtained a CFP's Raman

spectrum using used a LabRAM HR Evolution Raman microscope (Horiba, Ltd., Kyoto, Japan) with an excitation wavelength of 514 nm.

Preparation of anthraquinone-2-carboxylic acid-anchored carbon fiber paper. We purified a commercial CFP as mentioned above. To prepare anthraquinone-2-carboxylic acid-anchored carbon fiber paper (AQC/CFP), we immersed the CFP in an ethanolic solution containing 3 mM AQC for 24 h. Subsequently, we dried it at room temperature in air. We estimated the amount of surface-bound AQC using cyclic voltammetric analysis; the surface concentration of AQC (Γ_{AQC}) was estimated using **Equation 1**

$$\Gamma_{AQC} \, (\text{nmol cm}^{-2}) = Q \times (n \times F \times A)^{-1} \qquad (1)$$

where Q is the charge consumed for AQC's reduction, which was calculated from a cyclic voltammogram of the AQC-anchored CFP, n is the number of electrons transferred to AQC ($n = 2$), F is the Faraday constant (96,485 C mol^{-1}), and A is the geometrical surface area of the CFP. We obtained Nyquist plots of CFP and AQC/CFP electrodes using an impedance analyzer (ZIVE SP1, WonATech Co., Korea) at an AC potential amplitude of 10 mV. We fitted the Nyquist plots to calculate their charge-transfer resistances using a Zman software (WonATech Co., Korea).

Electrocatalytic production of H$_2$O$_2$. Electrocatalytic production of H$_2$O$_2$ was performed in a three-electrode configuration, which consisted of a working electrode, an Ag/AgCl (3 M NaCl) reference electrode, and a graphite rod counter electrode in a same compartment. An electrolyte solution was a potassium phosphate buffer (100 mM, pH 6.0, 2 mL). When we applied an electrical bias to this system, we used a potentiostat/galvanostat (WMPG 1000, WonATech Co., Korea).

When we investigate the pathway of the electrochemical production of H_2O_2, we supplemented 10 mM 1,4-benzoquinone ($O_2^{\bullet-}$ scavenger) into the electrolyte solution. All potentials have been quoted vs. reversible hydrogen electrode (RHE) according to **Equation 2**

$$E_{RHE} \text{ (V)} = E_{Ag/AgCl} \text{ (V)} + 0.209 + (0.059 \times \text{pH}) \tag{2}$$

After the electrochemical reaction, we collected a reaction solution, and mixed it with a colorimetric reagent solution [3.0 U HRP and 2 mM ABTS in a phosphate solution (100 mM, pH 5.0)]. We monitored its absorbance at 420 nm using a V-650 UV-Vis absorption spectrophotometer (JASCO Inc., Japan).

Electrobiocatalytic oxyfunctionalization reactions. We applied AQC/CFP-driven H_2O_2 production to r*Aae*UPO-mediated oxyfunctionalization reactions in a one-compartment, three-electrode configuration [working electrode: AQC/CFP, reference electrode: Ag/AgCl (3 M NaCl), counter electrode: CFP]. In the three-electrode configuration, an electrolyte solution was an O_2-rich KPi buffer (100 mM, pH 6.0, 2 mL) containing 50 nM r*Aae*UPO and 16 mM ethylbenzene. After the biocatalytic electrochemical reaction, we extracted oxyfunctionalized products using ethyl acetate, dried them over $MgSO_4$, and quantified them using a 7890A gas chromatograph (Agilent Technologies, USA) equipped with a flame ionization detector and a CP-Chirasil-Dex CB column (25 m × 0.32 mm × 0.25 μm).

Electrocatalytic regeneration of NADH. When we investigated the capability of CFP to reduce NAD^+ to NADH, we immersed a CFP electrode in a sodium phosphate buffer (100 mM, pH 7.5, 2 mL) containing NAD^+ and **M_{ox}** in three-electrode configuration. A reference electrode and counter

electrode were Ag/AgCl (3 M NaCl) and a graphite rod, respectively. We used a potentiostat/galvanostat (WMPG 1000, WonATech Co., Korea) to perform electrocatalytic analysis and controlled potential electrolysis. When we obtained linear sweep voltammograms and performed NADH regeneration tests, we added 0.25 mM M_{ox} and 1 mM NAD^+ in an O_2-depleted NaPi buffer. We quantified NADH using a V-650 UV-Vis absorption spectrophotometer (Jasco Inc., Japan). Nuclear magnetic resonance spectroscopic (NMR) analysis was performed to prove the formation of 1,4-NADH. We used a 400 MHz AVANCE III HD Nanobay (Bruker Corp., USA) equipped with a tunable multinuclear probe (PA BBO 400S1 BBF-H-D-05 Z plus).

Electrobiocatalytic amination and hydrogenation. When we performed enzymatic amination reactions, we added 500 nM GDH, 80 mM α-ketoglutarate, 250 mM NH_4^+, 0.25 mM M_{ox}, and 1 mM NAD^+ in an O_2-depleted NaPi buffer (100 mM, pH 7.5, 2 mL). A controlled potential electrolysis was performed in a three-electrode configuration [working electrode: CFP, reference electrode: Ag/AgCl (3 M NaCl), counter electrode: graphite rod]. The concentrations of α-ketoglutarate and L-glutamate were measured using a high-performance liquid chromatography (1260 Infinity liquid chromatography system, Agilent Technologies, USA) equipped with a variable wavelength detector and an Intersil C18 column. The eluent was a phosphoric acid aqueous solution (0.05 wt%), a flow rate was 1.0 mL min^{-1}, and detection wavelength was 214 nm. The retention times of α-ketoglutarate and L-glutamate were 9.5 and 3.1 min, respectively. When we drove enzymatic hydrogenation reactions, we added 5 μM TsOYE, 7 mM 2-methyl-2-cyclohexen-1-one, 10 mM $CaCl_2$, 20 mM NH_4^+, 0.25 mM M_{ox}, and 1 mM NAD^+ in an O_2-depleted triethanolamine (TEOA)-buffered solution (100 mM, pH 7.5, 2 mL). This experiment was also performed in a three-electrode configuration [working electrode: CFP, reference electrode: Ag/AgCl (3 M NaCl), counter

electrode: graphite rod]. The products of *Ts*OYE were quantified using a 7890A gas chromatograph (Agilent Technologies, USA) equipped with a flame ionization detector and a CP-Chirasil-Dex CB column (25 m × 0.32 mm × 0.25 μm).

Fabrication of photoanodes. We synthesized a hematite photoanode via solution-based processing and high temperature annealing. A commercial fluorine-doped tin oxide glass (TEC-7, Pilkington) was rinsed with acetone, isopropyl alcohol, and deionized water. To deposit a β-FeOOH nanostructure on the $F:SnO_2$ substrate, we prepared a precursor solution containing 150 mM $FeCl_3 \cdot 6H_2O$ and 1 M $NaNO_3$ in deionized water. The substrate was immersed in the solution and heated in a Lindberg/Blue M muffle furnace (Fisher Scientific Co., USA) at 100 ºC for 6 h. To transform β-FeOOH into α-Fe_2O_3, the electrode was annealed at 800 °C for 20 min. When we prepared a Zr:α-Fe_2O_3, we supplemented $ZrCl_4$ (0 to 2.5 mM) into the precursor solution, and followed the aforementioned method.

Preparation of PET-containing electrolyte solutions. Granular PET polymers (Sigma-Aldrich) or a commercial PET item (from Starbucks coffee company, or Coca-Cola company) was ground to microplastics (size ≤ *ca*. 5 mm) using a commercial coffee grinder. After we prepared an electrolyte solution by adding the microplastics in 5 M NaOH solution, we immediately conducted (photo)electrocatalytic reactions unless otherwise specified. We designated the solution "unpretreated PET solution", and its concentration was mentioned in a main text, figure, or figure legend. When we prepared a "pretreated PET solution", we immersed the microplastics in 5 M NaOH solution for 3 days at 353 K under dark conditions with stirring at 700 rpm unless otherwise specified; the amounts of the microplastics were mentioned in a main text, figure, or figure legend.

The concentration of ethylene glycol after pretreatment was approximately 200 mM as determined by quantitative nuclear magnetic resonance spectroscopy.

Photoelectrochemical reformation of PET. PEC reformation of PET was performed in a three-electrode configuration. The configuration consisted of a working electrode, an Hg/HgO (1 M NaOH) reference electrode, and a Pt counter electrode in a same compartment. The geometrical surface areas of photoanodes were 1.7 cm^2. When we performed controlled potential photoelectrolysis to drive PEC reformation PET, (i) the electrolyte volume was 2 mL unless otherwise specified, (ii) the light source was a xenon lamp (Newport Co., USA) that emitted a simulated solar light (light intensity: 1 sun), and (iii) an electrical bias was provided using a potentiostat/galvanostat (WMPG 1000, WonATech Co., Korea). All potentials have been quoted vs. reversible hydrogen electrode (RHE) according to the following equation (**Equation 3**)

$$E_{RHE} \text{ (V)} = E_{Hg/HgO} \text{ (V)} + 0.140 + (0.059 \times \text{pH}) \tag{3}$$

When we investigated which species (e.g., h$^+$, H$_2$O$_2$, OH$^•$) performed the waste-to-chemical conversion, we used a salt bridge to separate photoanodic and cathodic site, and added Na$_2$SO$_3$ (hole scavenger), sodium pyruvate (H$_2$O$_2$ scavanger), or tert-butyl alcohol (OH$^•$ scavanger) into an unpretreated PET solution (1 mg mL^{-1} PET microplastics, 5 M NaOH). When we tested the effect of O$_2$ on the PET reformation reaction, we purged N$_2$ gas into the anodic electrolyte solution before and during hematite-driven photoelectrochemical (PEC) reaction.

(Quantitative) nuclear magnetic resonance spectroscopy. A ^{1}H NMR spectrum was recorded using a 400 MHz AVANCE III HD Nanobay (Bruker Corp., USA) equipped with a tunable multinuclear probe (PA BBO 400S1 BBF-H-D-05 Z plus). We prepared a NMR sample (700 μL)

by diluting a reaction sample in a D_2O solvent (v/v, 9:1) containing maleic acid (quantification standard) and DSS (chemical shift standard); D_2O was used to provide an internal lock signal to correct drift in the magnetic field during the measurement. The NMR pulse sequence, relaxation delay, and temperature were zgesfpgp, 6 s, and 298 K. The molar concentration of analyte ($C_{analyte}$) in the sample was calculated according to **Equation 4**

$$C_{analyte} = \frac{I_{analyte} \times N_{standard}}{I_{standard} \times N_{analyte}} \times C_{standard}$$

$$(4)$$

where $I_{analyte}$ is the integral of the analyte peak, $I_{standard}$ is the integral of the standard peak, $N_{analyte}$ is the number of protons corresponding to the analyte peak, and $N_{standard}$ is the number of protons corresponding to the standard peak.

Photoelectrochemical biocatalysis. We connected a Zr:α-Fe_2O_3 photoanode and a CFP cathode (or AQC/CFP cathode) in two compartment using a salt bridge. We performed controlled potential photoelectrolysis using a xenon lamp (Newport Co., USA) and a potentiostat/galvanostat (WMPG 1000, WonATech Co., Korea); solar light was designed to be irradiated to an anodic site, not a cathodic site. The geometrical surface areas of the photoanode and the cathode were 1.7 and 1 cm^2, respectively, unless otherwise specified. An anodic electrolyte was a 5 M NaOH aqueous solution containing prehydrolysed PET microplastics; we prepared the microplastics by grinding Starbucks PET cup. The cathodic electrolyte was different according to the type of enzymes: (i) an O_2-enriched KPi buffer (100 mM, pH 6.0) containing rAaeUPO and substrate for oxyfunctionalization reactions, (ii) an O_2-depleted NaPi buffer (100 mM, pH 7.5) containing GDH, α-ketoglutarate, NH_4^+, **M_{ox}**, and NAD^+ for amination reactions, and (iii) an O_2-depleted TEOA buffer (100 mM, pH 7.5) containing TsOYE, substrate, Ca^{2+}, NH_4^+, **M_{ox}**, and NAD^+ for hydrogenation reactions. Gas chromatographic

analysis was used to quantify enzymatic products. We calculated the total turnver numbers of rAaeUPO, GDH and TsOYE according to **Equations 5, 6, and 7**:

$$\text{TTN}_{\text{r}AaeUPO} = \frac{\text{Maximum product concentration during enzymatic reaction}}{\text{Concentration of r}AaeUPO} \tag{5}$$

$$\text{TTN}_{\text{GDH}} = \frac{\text{Maximum product concentration during enzymatic reaction}}{\text{Concentration of GDH}} \tag{6}$$

$$\text{TTN}_{Ts\text{OYE}} = \frac{\text{Maximum product concentration during enzymatic reaction}}{\text{Concentration of }Ts\text{OYE}} \tag{7}$$

Conflicts of interest

The authors declare no competing interests.

Author contributions

J.K. and C.B.P. conceptualized the work. C.B.P. supervised the research. J.K. designed and analyzed the research. J.K. performed experimental works and wrote the manuscript. C.B.P. wrote the manuscript. J.J. performed and analyzed plastic treatments. J.J. synthesized rhodium-containing electron mediators. T.H. prepared old yellow enzymes. F.H. provided unspecific peroxygenases. All authors commented on the manuscript.

Data availability

The data supporting the findings of the study are available in the paper and its Supplementary Information.

References

1   Ryberg, M. W., Laurent, A. & Hauschild, M. in *Mapping of global plastics value chain and plastics losses to the environment*   (United Nations Environment Programme, 2018).

2   Adyel, T. M. Accumulation of plastic waste during COVID-19. *Science* **369**, 1314-1315 (2020).

3   Garcia, J. M. & Robertson, M. L. The future of plastics recycling. *Science* **358**, 870-872 (2017).

4   MacArthur, E. Beyond plastic waste. *Science* **358**, 843-843 (2017).

5   Ryan, P. G. in *Marine Anthropogenic Litter* (eds Melanie Bergmann, Lars Gutow, & Michael Klages) 1-25 (Springer International Publishing, 2015).

6   Law, K. L. & Thompson, R. C. Microplastics in the seas. *Science* **345**, 144-145 (2014).

7   Macarthur, D. E. in *The New Plastics Economy: Rethinking the Future of Plastics & Catalysing Action* (Ellen MacArthur Foundation, 2017).

8   Singh, A. K., Yasri, N., Karan, K. & Roberts, E. P. L. Electrocatalytic Activity of Functionalized Carbon Paper Electrodes and Their Correlation to the Fermi Level Derived from Raman Spectra. *ACS Appl. Energy Mater.* **2**, 2324-2336 (2019).

9   Molina-Espeja, P., Ma, S., Mate, D. M., Ludwig, R. & Alcalde, M. Tandem-yeast expression system for engineering and producing unspecific peroxygenase. *Enzyme Microb. Technol.* **73-74**, 29-33 (2015).

10   Pognon, G., Brousse, T., Demarconnay, L. & Bélanger, D. Performance and stability of electrochemical capacitor based on anthraquinone modified activated carbon. *J. Power Sources* **196**, 4117-4122 (2011).

11   Zhang, W. *et al.* Selective aerobic oxidation reactions using a combination of photocatalytic water oxidation and enzymatic oxyfunctionalizations. *Nat. Catal.* **1**, 55-62 (2018).

12   Kim, J. & Park, C. B. Shedding light on biocatalysis: photoelectrochemical platforms for solar-driven biotransformation. *Curr. Opin. Chem. Biol.* **49**, 122-129 (2019).

13   Lee, Y. W. *et al.* Unbiased biocatalytic solar-to-chemical conversion by FeOOH/BiVO$_4$/perovskite tandem structure. *Nat. Commun.* **9**, 4208 (2018).

14   Chaudhari, N., Landin, A. M. & Roper, S. D. A metabotropic glutamate receptor variant functions as a taste receptor. *Nat. Neurosci.* **3**, 113-119 (2000).

15   Sun, C. *et al.* l-Glutamate treatment enhances disease resistance of tomato fruit by inducing the expression of glutamate receptors and the accumulation of amino acids. *Food Chem.* **293**, 263-

270 (2019).

16   Hou, Y. & Wu, G. l-Glutamate nutrition and metabolism in swine. *Amino Acids* **50**, 1497-1510 (2018).

17   Wang, D. *et al.* Lignin-fueled photoelectrochemical platform for light-driven redox biotransformation. *Green Chem.* **22**, 5151-5160 (2020).

18   Son, E. J., Lee, Y. W., Ko, J. W. & Park, C. B. Amorphous Carbon Nitride as a Robust Photocatalyst for Biocatalytic Solar-to-Chemical Conversion. *ACS Sustain. Chem. Eng.* **7**, 2545-2552 (2019).

19   Kim, J. *et al.* Nicotinamide adenine dinucleotide as a photocatalyst. *Sci. Adv.* **5**, eaax0501 (2019).

20   Mifsud, M. *et al.* Photobiocatalytic chemistry of oxidoreductases using water as the electron donor. *Nat. Commun.* **5**, 3145 (2014).

21   Shen, S., Lindley, S. A., Chen, X. & Zhang, J. Z. Hematite heterostructures for photoelectrochemical water splitting: rational materials design and charge carrier dynamics. *Energy Environ. Sci.* **9**, 2744-2775 (2016).

22   Kim, J. H. & Lee, J. S. Elaborately Modified $BiVO_4$ Photoanodes for Solar Water Splitting. *Adv. Mater.* **31**, 1806938 (2019).

23   Liu, X., Wang, F. & Wang, Q. Nanostructure-based WO_3 photoanodes for photoelectrochemical water splitting. *PCCP* **14**, 7894-7911 (2012).

24   Uekert, T., Kasap, H. & Reisner, E. Photoreforming of Nonrecyclable Plastic Waste over a Carbon Nitride/Nickel Phosphide Catalyst. *J. Am. Chem. Soc.* **141**, 15201-15210 (2019).

25   Uekert, T., Kuehnel, M. F., Wakerley, D. W. & Reisner, E. Plastic waste as a feedstock for solar-driven H2 generation. *Energy Environ. Sci.* **11**, 2853-2857 (2018).

26   Iandolo, B., Wickman, B., Zorić, I. & Hellman, A. The rise of hematite: origin and strategies to reduce the high onset potential for the oxygen evolution reaction. *J. Mater. Chem. A* **3**, 16896-16912 (2015).

27   Xiao, M., Luo, B., Wang, Z., Wang, S. & Wang, L. Recent Advances of Metal-Oxide Photoanodes: Engineering of Charge Separation and Transportation toward Efficient Solar Water Splitting. *Solar RRL* **4**, 1900509 (2020).

28   Liao, P., Toroker, M. C. & Carter, E. A. Electron Transport in Pure and Doped Hematite. *Nano Lett.* **11**, 1775-1781 (2011).

29   Nam, D. H. *et al.* Water oxidation-coupled, photoelectrochemical redox biocatalysis toward mimicking natural photosynthesis. *Appl. Catal., B* **198**, 311-317 (2016).

30   Son, E. J. *et al.* Carbon Nanotube–Graphitic Carbon Nitride Hybrid Films for Flavoenzyme-Catalyzed Photoelectrochemical Cells. *Adv. Funct. Mater.* **28**, 1705232 (2018).

31   Choi, D. S., Kim, J., Hollmann, F. & Park, C. B. Solar-Assisted eBiorefinery: Photoelectrochemical Pairing of Oxyfunctionalization and Hydrogenation Reactions. *Angew. Chem. Int. Ed.* **59**, 15886-15890 (2020).

32   Choi, D. S. *et al.* Bias-Free In Situ H_2O_2 Generation in a Photovoltaic-Photoelectrochemical Tande

m Cell for Biocatalytic Oxyfunctionalization. *ACS Catal.* **9**, 10562-10566 (2019).

33   Burek, B. O. *et al.* Photoenzymatic Hydroxylation of Ethylbenzene Catalyzed by Unspecific Peroxy genase: Origin of Enzyme Inactivation and the Impact of Light Intensity and Temperature. *Chem CatChem* **11**, 3093-3100 (2019).

34   Lee, S. H., Choi, D. S., Kuk, S. K. & Park, C. B. Photobiocatalysis: Activating Redox Enzymes by Direct or Indirect Transfer of Photoinduced Electrons. *Angew. Chem. Int. Ed.* **57**, 7958-7985 (2018).

35   Kim, J. *et al.* Robust $FeOOH/BiVO_4/Cu(In, Ga)Se_2$ tandem structure for solar-powered biocatalytic CO_2 reduction. *J. Mater. Chem. A* **8**, 8496-8502 (2020).

36   Kuk, S. K. *et al.* CO_2-Reductive, Copper Oxide-Based Photobiocathode for Z-Scheme Semi-Artificial Leaf Structure. *ChemSusChem* **13**, 2940-2944 (2020).

37   Ren, Y. *et al.* Strategies to suppress hydrogen evolution for highly selective electrocatalytic nitrogen reduction: challenges and perspectives. *Energy Environ. Sci.* **14**, 1176-1193 (2021).
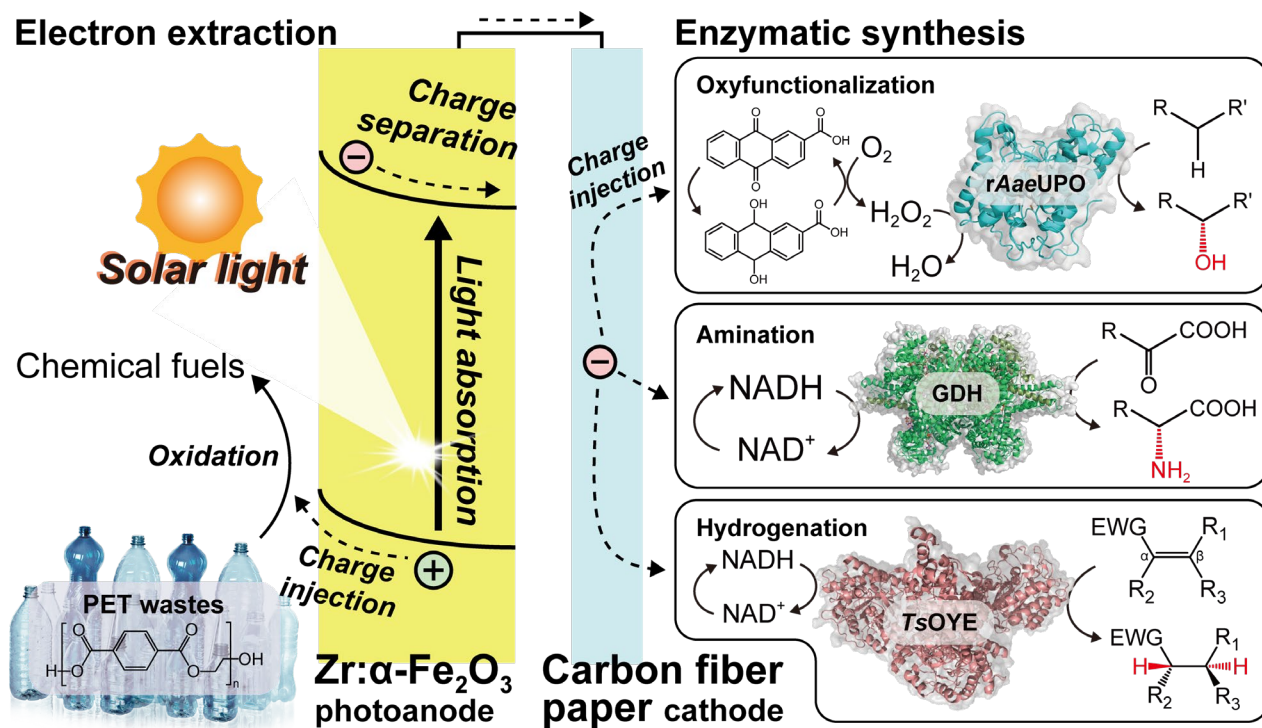
Fig. 1: Schematic diagram of solar-powered photoelectrochemical (PEC) biosynthetic reactions using nonrecyclable real-world poly(ethylene terephthalate) (PET) microplastics. A carbon fiber paper (CFP)-based cathodes reduce (i) O_2 to H_2O_2 for biocatalytic oxyfunctionalization and (ii) NAD^+ to 1,4-NADH for enzymatic amination and asymmetric hydrogenation. For the bioelectrocatalytic synthesis, a Zr-doped hematite (Zr:α-Fe$_2$O$_3$) photoanode extracts electrons from hydrolyzed PET solutions from post-consumer PET wastes of Starbucks and Coca-Cola companies. The biocatalytic PEC systems produce value-added compounds at both electrodes with excellent total turnover numbers of enzymes.
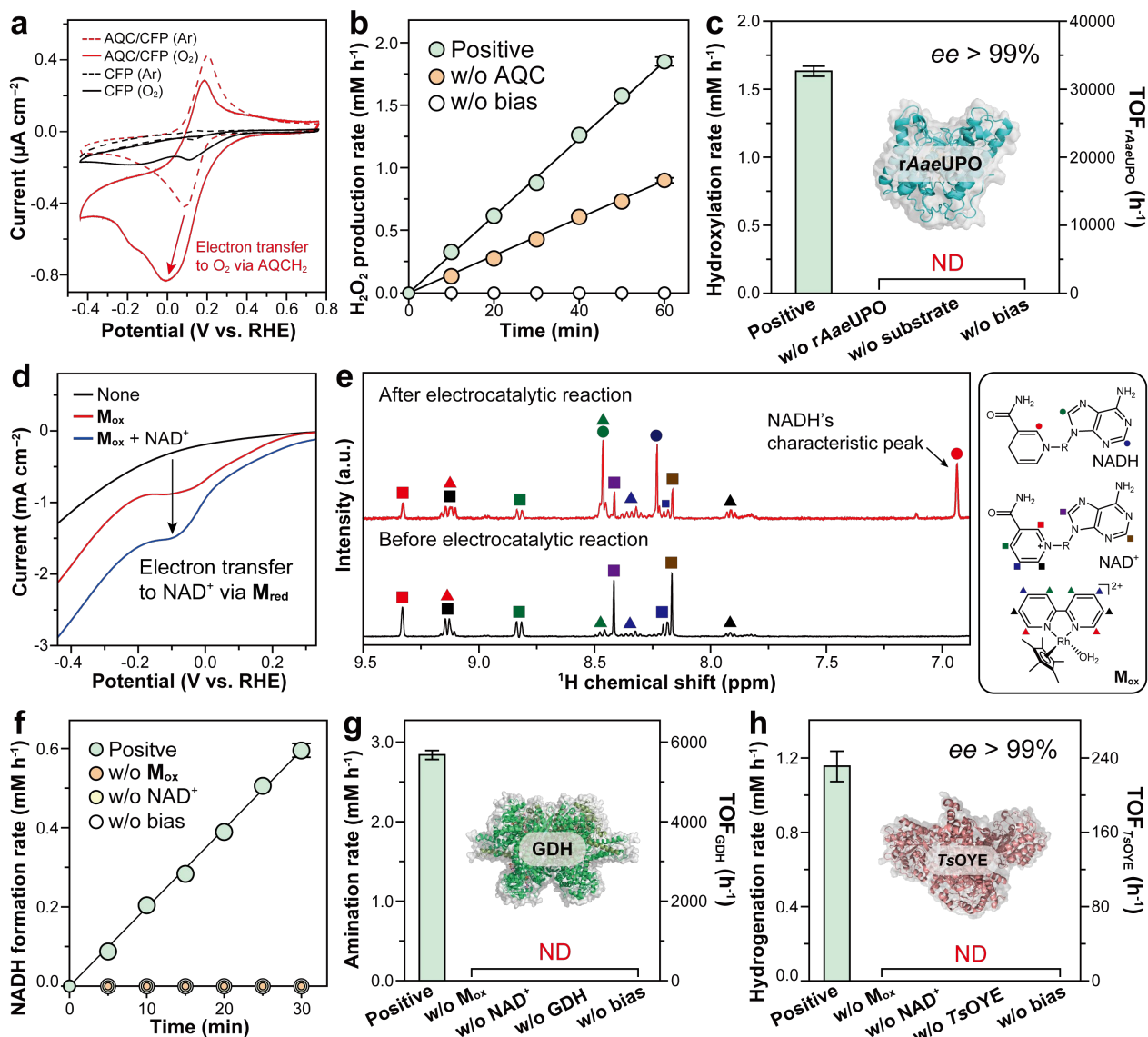
Fig. 2: Bioelectrocatalytic synthesis using CFP-based materials. (**a**) Cyclic voltammograms of AQC/CFP and CFP cathodes under O_2 or Ar-enriched environments. Electrolyte solution: a KPi buffer (100 mM, pH 6.0). (**b**) Time profiles of electrocatalytic production of H_2O_2. Electrolyte solution: an O_2-rich KPi buffer (100 mM, pH 6.0). (**c**) Biocatalytic electrochemical hydroxylation reaction using AQC/CFP and r*Aae*UPO. (**d**) Linear sweep voltammograms for NAD^+ reduction. (**e**) ^{1}H nuclear magnetic resonance spectra before and after electrocatalytic reaction at -0.2 V_{RHE}. Molecular structures of NADH, NAD^+, and M_{ox} are shown in the right panel. Reaction time: 40 min. (**f**) Electrochemical production of 1,4-NADH from NAD^+ using CFP cathode. (**g**) A series of control experiments in bioelectrochemical amination reaction using GDH. (**h**) Control experiments in enzymatic electrochemical hydrogenation reaction using *Ts*OYE. Working electrode in (**d-h**): CFP. Geometrical surface areas of cathodes in (**a-h**): 1 cm^2. Reaction temperature in (**a-h**): 303 K. Applied bias in (**b, c**): 0.16 V_{RHE}. Applied bias in (**e-h**): -0.2 V_{RHE}. Scan rate in (**a, d**): 25 mV s^{-1}. ND: not detected. Error bar: standard deviation (*n* = 3).
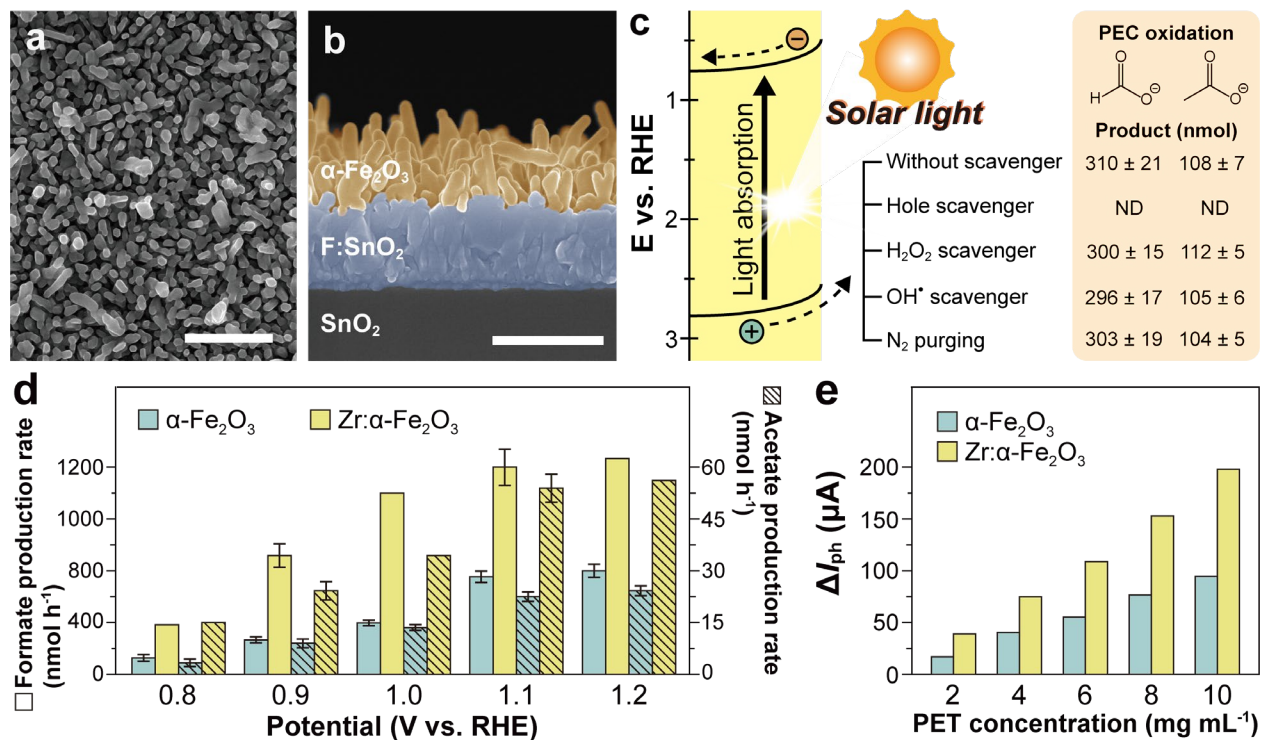
Fig. 3: PEC reformation of PET microplastics using Fe₂O₃-based photoanodes. (**a**) Plan-view SEM image of α-Fe₂O₃ electrode. Scale bar: 1000 nm. (**b**) Cross-sectional SEM image of the photoelectrode. Scale bar: 800 nm. (**c**) Effects of various scavengers and N₂ molecules on the PEC oxidation of PET microplastics for 12 h at 1.0 V_RHE. Concentrations of scavengers: 300 mM Na₂SO₃ (hole scavenger), 300 mM sodium pyruvate (H₂O₂ scavenger), and 300 mM *tert*-butyl alcohol (OH• radical scavenger). We separated photoanodic and cathodic sites using a salt bridge. (**d**) Potential-dependent production rates of formate and acetate driven by α-Fe₂O₃ and Zr:α-Fe₂O₃ photoanodes. (**e**) Comparison of ΔI_ph of the hematite-based photoanodes at 1.1 V_RHE. ΔI_ph ≡ I_ph (specific concentration of PET) − I_ph (0 mg mL⁻¹ PET). Light source in (**c-e**): solar simulator (AM 1.5G, 100 mW cm⁻²). Electrolyte solutions: (**c**) unpretreated PET solution (1 mg mL⁻¹ PET microplastics, 5 M NaOH), (**d**) pretreated PET solution (5 mg mL⁻¹ PET microplastics, 5 M NaOH), and (**e**) pretreated PET solution (PET microplastics, 5 M NaOH). Temperature in (**c-e**): 303 K. ND: not detected. Error bar: standard deviation (*n* = 3).
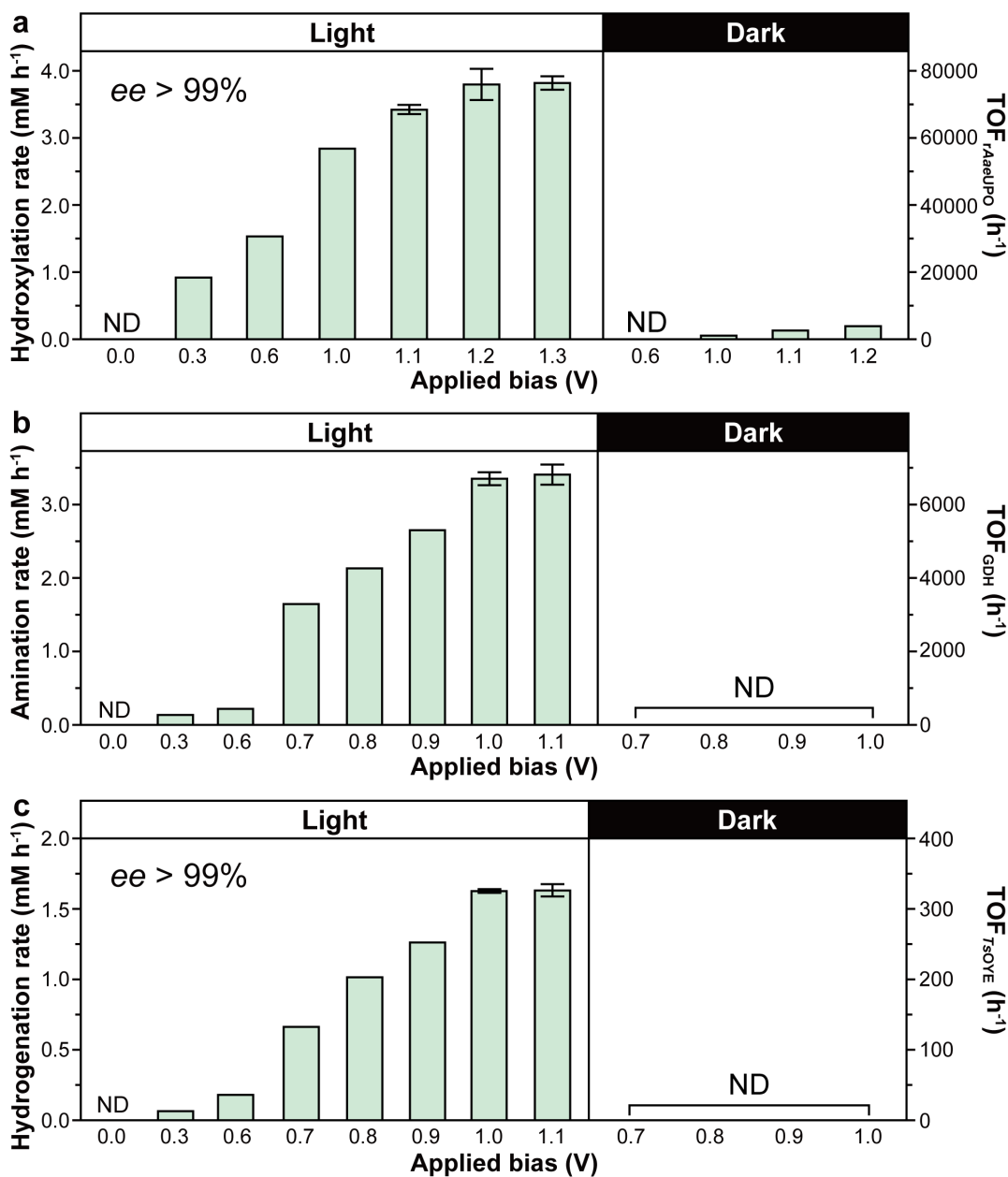
Fig. 4: Biocatalytic photoelectrochemical synthesis using real-world microplastics. Bias-dependent enzymatic reactions driven by (**a**) r*Aae*UPO, (**b**) GDH, and (**c**) *Ts*OYE. Cathodic electrolyte in (**a**): 50 nM r*Aae*UPO and 16 mM ethylbenzene in an O_2-rich KPi buffer (100 mM, pH 6.0). Cathodic electrolyte in (**b**): 500 nM GDH, 80 mM α-ketoglutarate, 250 mM NH_4^+, 0.25 mM $\mathbf{M_{ox}}$, and 1 mM NAD^+ in an O_2-depleted NaPi buffer (100 mM, pH 7.5). Cathodic electrolyte in (**c**): 5 μM *Ts*OYE, 7 mM 2-methyl-2-cyclohexen-1-one, 10 mM $CaCl_2$, 20 mM NH_4^+, 0.25 mM $\mathbf{M_{ox}}$, and 1 mM NAD^+ in an O_2-depleted TEOA-buffered solution (100 mM, pH 7.5). Cathode in (**a**): AQC/CFP electrode. Cathodes in (**b, c**): CFP electrode. Anodic electrolyte in (**a-c**): pretreated PET solution (50 mg mL^{-1} PET microplastics, 5 M NaOH) using Starbucks PET disposable cups. Light condition in (**a-c**): 1 sun (AM 1.5G, 100 mW cm^{-2}). We irradiated solar light to the anodic site, not the cathodic site. Temperature: 303 K.
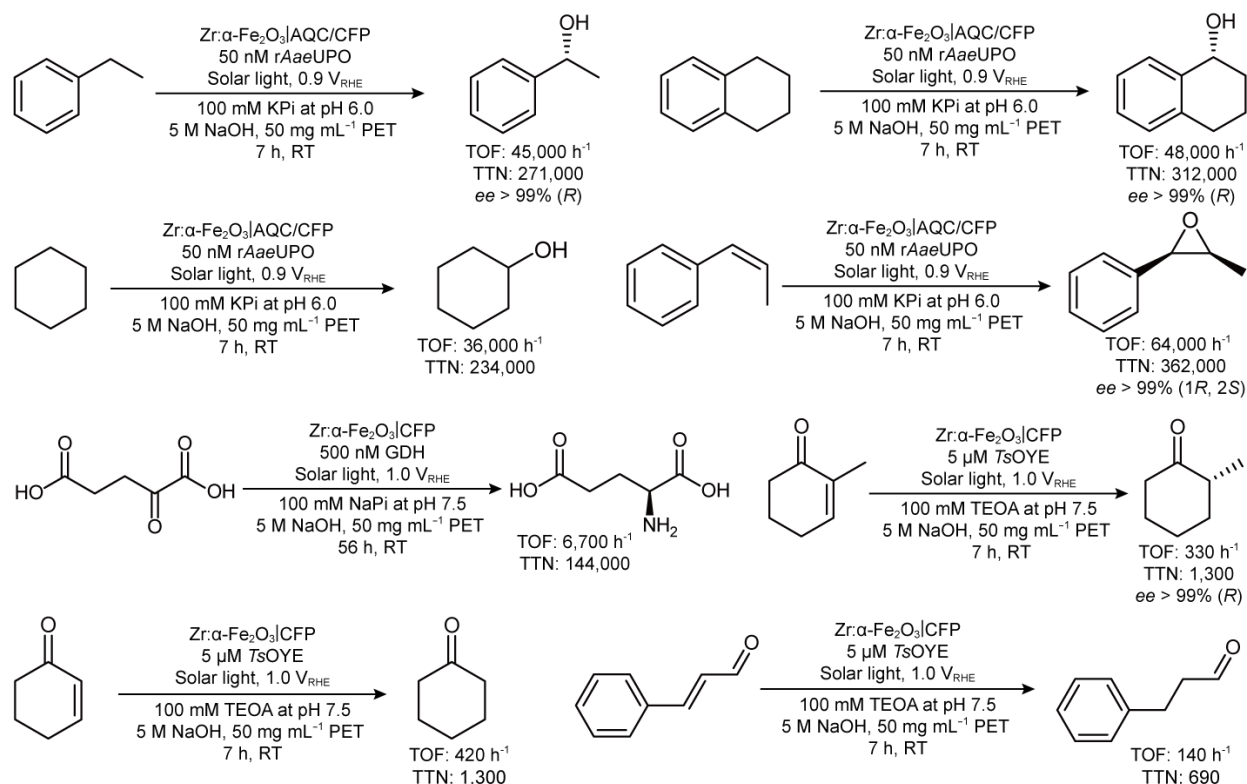
Fig. 5: Substrate scope of biocatalytic PEC reactions employing real-world PET microplastics. Cathodic electrolyte for r*Aae*UPO reaction: 50 nM r*Aae*UPO and 16 mM substrate in an O_2-rich KPi buffer (100 mM, pH 6.0). Cathodic electrolyte for GDH reaction: 500 nM GDH, 80 mM α-ketoglutarate, 250 mM NH_4^+, 0.25 mM M_{ox}, and 1 mM NAD^+ in an O_2-depleted NaPi buffer (100 mM, pH 7.5). Cathodic electrolyte for *Ts*OYE catalysis: 5 μM *Ts*OYE, 7 mM substrate, 10 mM $CaCl_2$, 20 mM NH_4^+, 0.25 mM M_{ox}, and 1 mM NAD^+ in an O_2-depleted TEOA-buffered solution (100 mM, pH 7.5). Anodic electrolyte: pretreated PET solution (50 mg mL^{-1} PET microplastics, 5 M NaOH) using Starbucks PET disposable cups. Light condition: 1 sun (AM 1.5G, 100 mW cm^{-2}). Temperature: 303 K.
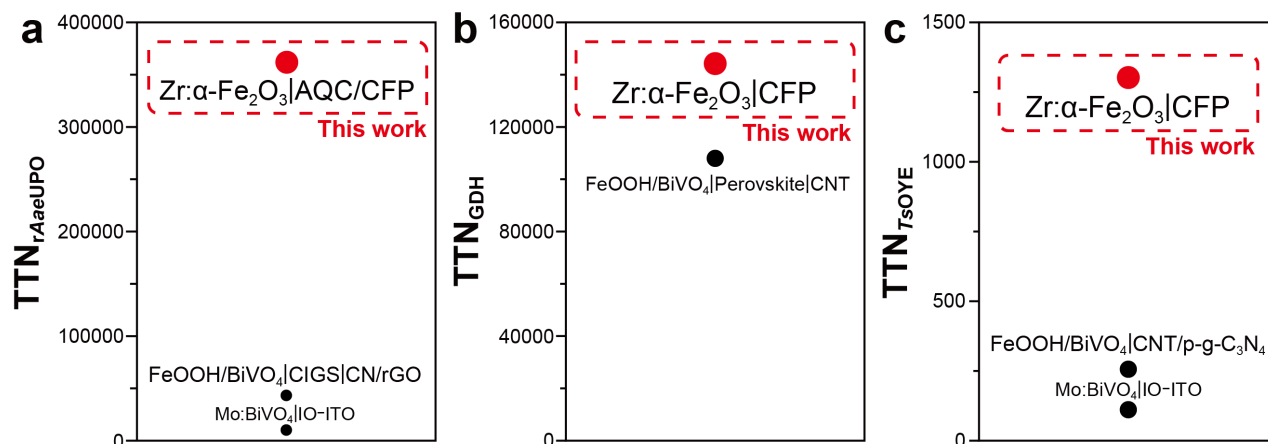
Fig. 6: Comparison of total turnover numbers (TTNs) of enzymes of state-of-the-art biocatalytic PEC systems. List of redox enzymes activated by PEC systems: (**a**) rAaeUPO,[31,32] (**b**) GDH,[13] and (**c**) TsOYE[30,31]. References: FeOOH/BiVO4|CIGS|CN/rGO,[32] Mo:BiVO4|IO-ITO,[31] FeOOH/BiVO4|Perovskite|CNT,[13] FeOOH/BiVO4|CNT/p-g-C3N4[30]. FeOOH/BiVO4: FeOOH-deposited BiVO4. CIGS: Cu(In,Ga)Se2. CN/rGO: graphitic carbon nitride/reduced graphene oxide hybrid. Mo:BiVO4: Mo-doped BiVO4. IO-ITO: inverse opal-structured indium tin oxide. CNT: carbon nanotube. CNT/p-g-C3N4: protonated graphitic carbon nitride/carbon nanotube hybrid.